
MODEM: A Morton-Order Degradation Estimation Mechanism for Adverse Weather Image Recovery

Hainuo Wang, Qiming Hu, Xiaojie Guo*

College of Intelligence and Computing, Tianjin University, Tianjin 300350, China
hainuo@tju.edu.cn huqiming@tju.edu.cn xj.max.guo@gmail.com

Abstract

Restoring images degraded by adverse weather remains a significant challenge due to the highly non-uniform and spatially heterogeneous nature of weather-induced artifacts, *e.g.*, fine-grained rain streaks versus widespread haze. Accurately estimating the underlying degradation can intuitively provide restoration models with more targeted and effective guidance, enabling adaptive processing strategies. To this end, we propose a Morton-Order Degradation Estimation Mechanism (MODEM) for adverse weather image restoration. Central to MODEM is the Morton-Order 2D-Selective-Scan Module (MOS2D), which integrates Morton-coded spatial ordering with selective state-space models to capture long-range dependencies while preserving local structural coherence. Complementing MOS2D, we introduce a Dual Degradation Estimation Module (DDEM) that disentangles and estimates both global and local degradation priors. These priors dynamically condition the MOS2D modules, facilitating adaptive and context-aware restoration. Extensive experiments and ablation studies demonstrate that MODEM achieves state-of-the-art results across multiple benchmarks and weather types, highlighting its effectiveness in modeling complex degradation dynamics. Our code will be released at here.

1 Introduction

Computer vision systems are increasingly integral to critical applications, such as autonomous driving [41, 1] and intelligent surveillance [39, 59], demanding reliable performance in diverse environments. However, their effectiveness deteriorates significantly under adverse weather conditions, such as rain [11, 32, 46, 62, 65], haze [63, 64, 16, 51, 60, 70, 71], and snow [28, 35, 48, 73], which introduce complex visual artifacts and obscure critical scene information. Thus, effectively restoring clear images from such weather-degraded inputs is essential to boost the robustness and safety of modern computer vision technologies in real-world deployments.

Early task-specific methods [2, 4, 18, 49, 50, 22, 24] largely rely on physical models or hand-crafted statistical priors tailored to individual weather phenomena. Due to the limited feature representation capabilities, these schemes are brittle in the face of complex scenes or deviations from assumed degradation patterns. With the advent of deep learning, numerous deep networks have achieved impressive performance by training on large-scale datasets for specific tasks such as image deraining [11, 32, 46, 62, 65, 5, 31, 58, 70], dehazing [63, 64, 16, 51, 60, 70, 71], or desnowing [28, 35, 48, 73]. These models excel at implicitly learning the inverse mapping through extensive supervision. But their highly specialized nature necessitates separate models for each weather condition, severely limiting scalability and practical deployment in unconstrained environments.

Recently, much attention has been directed toward unified or multi-task frameworks designed to cope with various weather conditions within a single model [78, 56, 8, 30, 44, 54, 66]. These

*Corresponding Author

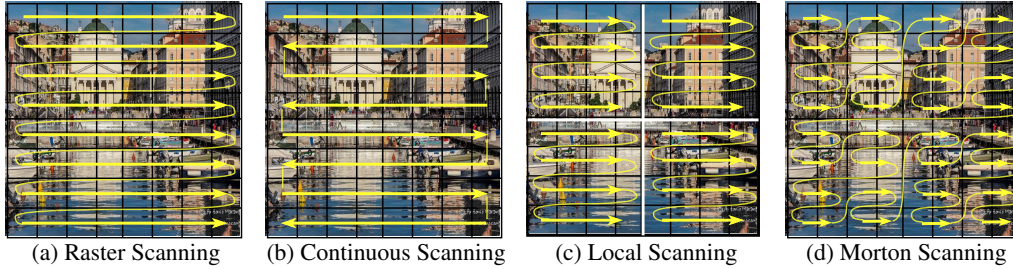


Figure 1: Comparison of various image scanning methods. (a) Raster Scanning. (b) Continuous Scanning. (c) Local Scanning. (d) Morton Scanning, which can better preserve spatial locality of neighboring pixels in the resulting 1D sequence, beneficial for capturing contextual information.

approaches adopt a variety of sophisticated strategies, including architecture search for optimal generalization [30], disentanglement of weather-shared and weather-specific representations [78], knowledge distillation and regularization [8], generative diffusion modeling [44], learned priors or codebooks [66], and transformer-based architectures that offer strong global modeling capabilities [56, 54]. Although these models mark notable progress and offer broader applicability, they still struggle with the challenge of modeling the inherently distinct and often highly spatially heterogeneous characteristics of different weather degradations. For example, haze tends to cause smooth intensity attenuation, whereas rain streaks and snowflakes introduce sharp, local occlusions with specific structural patterns. Most existing architectures lack dedicated degradation estimation mechanisms to explicitly model and leverage these fine-grained, spatially variant degradation patterns, which undermines their performance in real-world deployment. Therefore, *effective estimation of spatially variant degradation characteristics, encompassing both global trends and local structures, as guidance is critical for adaptive and context-aware restoration under dynamic weather conditions.*

For an element (*e.g.*, pixel) of a degraded image, its degradation characteristic can be regarded as a latent “state” within a degradation space, encapsulating the influence of adverse weather on its visual appearance. These states evolve spatially, governed by both local (*e.g.*, rain streaks) and non-local patterns (*e.g.*, drifting fog). This perspective naturally lends itself to State Space Modeling (SSM) [12]. The connection between the image degradation modeling and SSM is formally given in Sec. 3. By treating degradation as a structured sequence of evolving states, SSM can capture long-range contextual dependencies while maintaining sensitivity to local features. When coupled with degradation estimation mechanisms, SSM empowers the restoration process to be contextually aware and spatially adaptive, effectively aligning restoration strategies with the heterogeneous and scene-specific nature of weather-induced artifacts.

Motivated by the above insight, we propose a novel Morton-Order Degradation Estimation Mechanism (MODEM) that **estimates** degradation state via SSM and **guides** adaptive restoration in degraded images. At the heart of MODEM lies the Morton-Order 2D-Selective-Scan Module (MOS2D), which integrates SSM with Morton-coded spatial traversal. Unlike conventional raster scanning, the Morton-order scan follows a hierarchical, locality-preserving sequence [40, 25, 43, 23] that enables structured and efficient modeling of both local and long-range dependencies, as shown in Fig. 1(d). To complement MOS2D, we further introduce a Dual Degradation Estimation Module (DDEM), designed to extract two complementary forms of degradation information from the input: (i) a global degradation representation that encapsulates high-level weather characteristics such as type and severity, and (ii) a set of spatially adaptive kernels that encode local degradation structures and variations. These dual degradation representations are then utilized to dynamically modulate the restoration process. Specifically, the global representation adaptively influences feature transformations within MODEM, while the spatially adaptive kernels guide the matrix construction within MOS2D, refining the spatial dependencies captured along the Morton-order sequence. This dual-modulation strategy equips the restoration network with both global awareness and local sensitivity, thereby delivering more precise and effective restoration. Our primary contributions can be summarized as follows:

- We propose a novel Morton-Order Degradation Estimation Mechanism that introduces the MOS2D module, which integrates Morton-coded spatial ordering with selective state space modeling to effectively capture spatially heterogeneous weather degradation dynamics.
- We design a Dual Degradation Estimation Module that jointly estimates global degradation descriptors and spatially adaptive kernels. These two complementary representations are used to dynamically modulate MOS2D, allowing contextually aware and spatially adaptive restoration.

- Extensive experiments and ablation studies are conducted to demonstrate the effectiveness of the proposed MODEM, and its superiority over other state-of-the-art competitors in restoring images under diverse and complex adverse weather conditions.

2 Related Work

This section briefly reviews representative approaches to single adverse weather restoration including rain streak removal, raindrop removal, haze removal and snow removal, as well as unified all-in-one models. Additionally, recent advances in SSM-based image restoration techniques are also discussed.

Rain Streak Removal. Traditional rain streak removal methods typically relied on image decomposition [24] or tensor-based priors [22]. With the advent of deep learning, various models have emerged, like the deep detail network for splitting rain details [11], recurrent networks for context aggregation in single images [31], and spatio-temporal aggregation in videos [32]. Further developments include uncertainty-guided multi-scale designs [65], density-aware architectures [70], spatial attention [58], joint detection-removal frameworks [62], and NAS-based attentive schemes [5].

Raindrop Removal. Early raindrop removal efforts addressed specific scenarios [10] or adherent raindrops in videos [67]. Deep learning subsequently provided more generalizable solutions, including learning from synthetic photorealistic data [17], using attention-guided GANs for realistic inpainting [46], and dedicated networks for visibility through raindrop-covered windows [47]. General restoration architectures like Dual Residual Networks [33] are also applicable, with advanced dual attention-in-attention models [72] tackling joint rain streak and raindrop removal.

Haze Removal. Traditional image dehazing methods often utilized statistical priors the Dark Channel Prior (DCP) [18], non-local similarity techniques [4], or multi-scale fusion [2]. But these approaches faced robustness issues in diverse hazy scenes due to strong underlying assumptions. Deep learning has since become dominant, with methods focusing on estimating transmission and atmospheric light, sometimes using depth awareness [63] or unpaired learning via decomposition [64]. Other approaches tackle haze density variations [70, 71], domain adaptation [51], and contrastive learning [60].

Snow Removal. While specific traditional priors for snow removal are less common compared to other weather conditions, principles from general image restoration were often adapted. Deep learning solutions for desnowing have gained traction, often involving networks sensitive to image context [35] or explicitly leveraging semantic segmentation and depth estimation as priors [73]. Techniques inspired by classical methods like matrix decomposition have also been integrated into deep frameworks [48], alongside methods developed for online processing of surveillance videos [28].

While these specialized models excel under specific weather conditions, their limited generalization requires separate models for each degradation type, hindering real-world practicality.

Unified Adverse Weather Restoration. To mitigate the inefficiency of deploying multiple models for complex weather conditions, unified models have been devised [78, 56, 8, 30, 44, 54, 66]. However, these unified ones face a fundamental challenge that *the degradation space covered by unified models is exponentially larger than that of weather-specific counterparts*, substantially increasing the complexity of accurate modeling and generalization. To tackle this, existing approaches employ different strategies to learn more generalizable representations. Early efforts included using NAS to find a unified structure [30] and leveraging Transformers like TransWeather [56] for their global context modeling. Others focused on training strategies, such as two-stage knowledge learning with multi-contrastive regularization [8]. More recent works have explored disentangling weather-general and weather-specific features [78]), adapting powerful generative models like diffusion models [44]), incorporating learned codebook priors [66]), and enhancing Transformers with global image statistics like Histoformer [54]. These methods showcase a trend towards more sophisticated and adaptive unified restoration. Despite progress, the unified models still struggle to effectively capture the diverse and spatially heterogeneous characteristics of different weather phenomena.

SSM-based Image Restoration. Recent State Space Models (SSMs) [13, 12], notably Mamba [12] with its selective scan mechanism, offer efficient long-sequence modeling and have rapidly permeated computer vision [42, 77, 34, 38, 53]. Inspired by these advancements, SSMs are increasingly applied to image restoration. General frameworks like MambaIR [15], VMambaIR [52], and CU-Mamba [9] demonstrate the potential of Mamba-based models as strong baselines. Specific low-level vision applications have also seen tailored solutions. For example, WaterMamba [14] has been developed

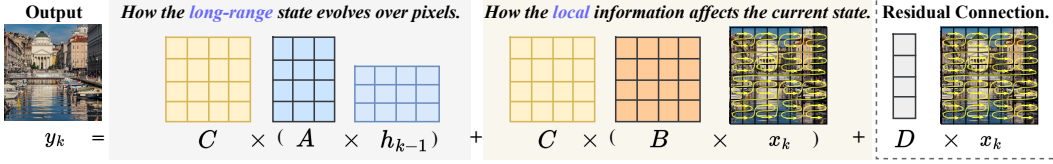


Figure 2: Connection between MODEM and SSM.

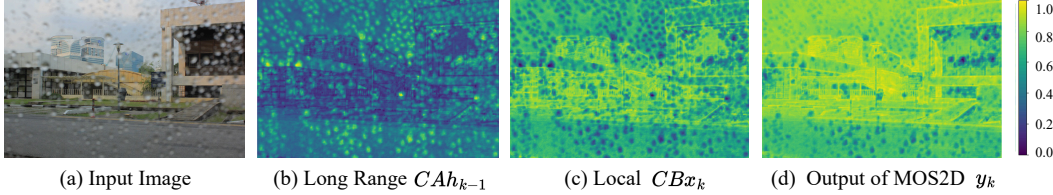


Figure 3: With respect to a sample (a), (b)-(d) visualize the long-range CAh_{k-1} , (c) local CBx_k , and (d) output of MOS2D y_k , respectively.

for underwater image enhancement, and IRSRMamba [19] addresses infrared super-resolution. Low-light image enhancement has been tackled by models like RetinexMamba [3] and LLEMamba [74], while efficient SSM designs have been proposed for image deblurring [26]. In image deraining, notable works include FourierMamba [27] and FreqMamba [75]. These efforts underscore the growing success of SSMs in addressing image restoration challenges. Our work builds upon this trend, leveraging SSMs for adaptive modeling of spatially heterogeneous weather degradations.

3 Bridging Image Degradation Estimation and State Space Modeling

Restoring images corrupted by adverse weather is inherently a highly ill-posed problem. In general, the relationship between an observed degraded image x and its clean version y can be modeled as:

$$x = \text{Degrade}(y, \theta := \{\theta_G, \theta_L\}) \Leftrightarrow y = \text{Restore}(x, \theta := \{\theta_G, \theta_L\}), \quad (1)$$

where $\text{Degrade}(\cdot, \theta)$ designates a complex, often spatially varying weather degradation function parameterized by θ . By considering the spatial influence of degradation, the parameter set (θ) can be partitioned into long-range/global degradation (θ_G , *e.g.* atmospheric haze) and local one (θ_L , *e.g.* rain streak). The objective is to recover the latent clean y from the degraded observation x . The core challenge lies in the fact that both the degradation process and the artifacts are unknown and can vary significantly across scenes and weather types. Thus, estimating the degradation characteristic θ and constructing the function $\text{Restore}(\cdot, \theta)$ in Eq. (1), is central to solving the problem.

We propose that State Space Models (SSMs) [12] offer a suitable and robust framework for this degradation estimation task. Recall the core recurrence of a discrete-time SSM:

$$h_k = Ah_{k-1} + Bx_k, \quad y_k = Ch_k + Dx_k, \quad (2)$$

where x_k is the input Morton-order sequence at step k , h_k is the latent hidden state summarizing historical context, and y_k is the output. The matrices A , B , and C are learnable parameters that define the SSM’s dynamics and output mapping. Please notice that the term Dx_k is a practical (non-theoretical) addition for training ease, which is analogous to residual connection. To better understand how the state dynamics contribute to the output y_k , we can analyze the system by omitting the residual Dx_k and substitute h_k into the $y_k = Ch_k$ part, as follows:

$$y_k = CAh_{k-1} + CBx_k. \quad (3)$$

By comparing Eq. (1) with Eq. (3), we interpret SSM components as degradation estimators, as illustrated in Fig. 2. The term CAh_{k-1} conceptually models the long-range, spatially propagated degradation context, as shown in Fig. 3(b). The previous hidden state h_{k-1} summarizes accumulated degradation cues (*e.g.*, overall haze level, rain intensity) along the Morton-order scan path. The state transition matrix A then models how these summarized characteristics evolve or persist as the scan progresses spatially (*e.g.*, the smooth attenuation of visibility due to widespread haze or the consistent statistical properties of rain streaks over a larger area.). It essentially dictates “how the long-range state evolves over pixels” as noted in Fig. 2. The output matrix C then translates this evolved context Ah_{k-1} into a contribution to the current output y_k , reflecting broader, non-local degradation patterns.

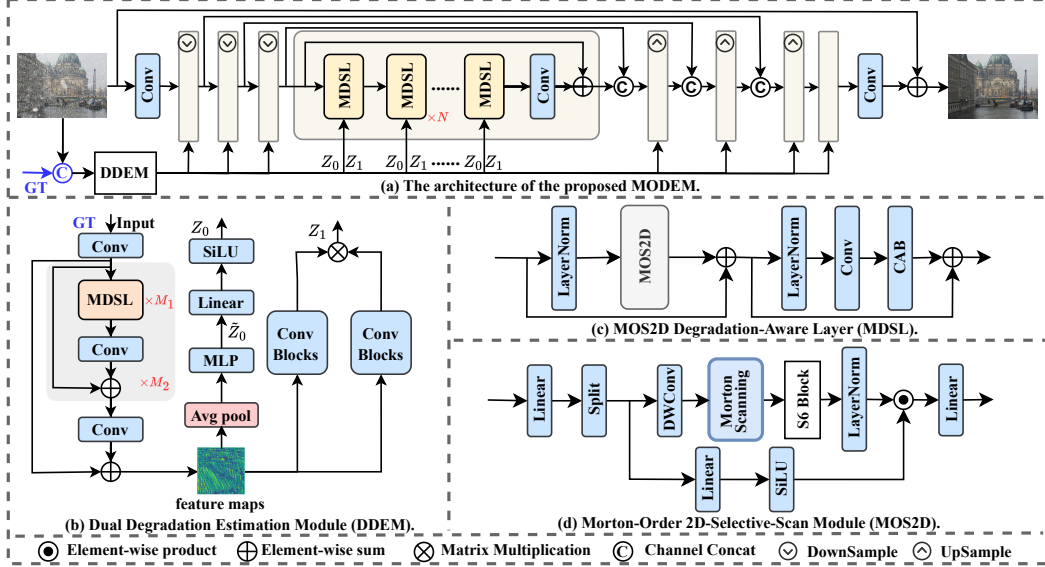


Figure 4: (a) Overall architecture of MODEM. (b) The DDEM for extracting global descriptor Z_0 and adaptive degradation kernel Z_1 degradation priors. (c) The MDSL incorporating the core MOS2D module (d) within a residual block. The blue-colored components indicate elements exclusive to the first training stage. N , M_1 , M_2 denote the number of the corresponding module, respectively.

Concurrently, the $Cb x_k$ term accounts for the impact of the immediate, local input features x_k , as visualized in Fig. 3(c). The input matrix B determines “how the local information affects the current state” (Fig. 2), allowing features from x_k (e.g., local degradation artifacts like dense fog patches, or crucial local image content like fine textures/sharp edges) to directly influence the current hidden state h_k . This enables the SSM to react to fine-grained local evidence, with C projecting this locally-informed component into y_k for specific adjustments based on immediate observations.

4 Morton-Order Degradation Estimation Mechanism

The Morton-Order Degradation Estimation Mechanism (MODEM), depicted in Fig. 4(a), employs a two-stage training strategy. During the first stage, the Dual Degradation Estimation Module (DDEM), shown in Fig. 4(b), utilizes both the degraded image I_{LQ} and its corresponding ground-truth I_{GT} to learn an accurate mapping to degradation priors: a global descriptor Z_0 and adaptive degradation kernel Z_1 . In the second stage, DDEM processes only the degraded input I_{LQ} , with its estimation of Z_0 and Z_1 being supervised by the frozen first stage. The priors, Z_0 and Z_1 , are injected into MODEM’s main restoration backbone in Fig. 4(a). This backbone is comprised of N stacked MOS2D Degradation-Aware Layers (MDSLs), detailed in Fig. 4(c). Each MDSL leverages the Morton-Order 2D-Selective-Scan module (MOS2D), shown in Fig. 4(d) and Fig. 5, to adaptively modulate features based on the degradation priors Z_0 and Z_1 .

4.1 Dual Degradation Estimation Module (DDEM)

The Dual Degradation Estimation Module (DDEM), shown in Fig. 4(b), extracts global degradation descriptor Z_0 and adaptive degradation kernel Z_1 . In the first stage, DDEM processes the degraded image I_{LQ} and ground-truth I_{GT} . Otherwise, it uses only I_{LQ} . The input undergoes several MOS2D Degradation-Aware Layers (MDSLs) to extract degradation feature map $F \in \mathbb{R}^{H \times W \times C_d}$. Subsequently, the global descriptor Z_0 and adaptive kernels Z_1 are derived from F as follows:

$$\tilde{Z} = \text{MLP}(\text{AvgPool}(F)), \quad Z_0 = \sigma(\text{Linear}(\tilde{Z})), \quad Z_1 = \text{Conv}(F) \times \text{Conv}(F)^T, \quad (4)$$

where $\sigma(\cdot)$ denotes the SiLU activation function, $\tilde{Z} \in \mathbb{R}^{4C_d}$ will be used for degradation supervision. These priors $Z_0 \in \mathbb{R}^{C_d}$ and $Z_1 \in \mathbb{R}^{C_{d1} \times C_{d2}}$ then guide the main restoration network.

MOS2D Degradation-Aware Layers (MDSL). The iterative application of MDSL enhances sensitivity to degradation patterns, yielding enriched feature maps. For the feature map F_i at the i -th MDSL,

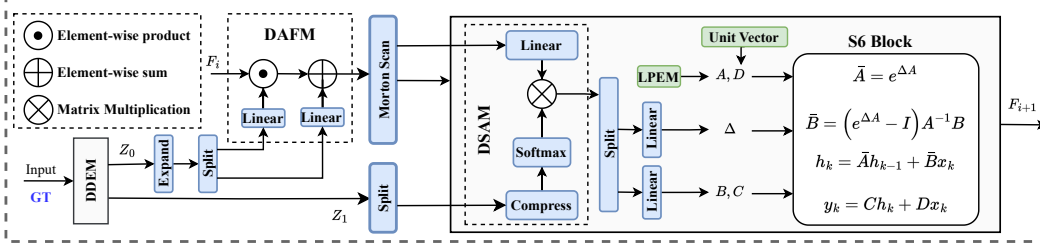


Figure 5: Detailed illustration of the degradation modulation mechanism within a MOS2D module in the main restoration backbone, which employs the Degradation-Adaptive Feature Modulation (DAFM) and Degradation-Selective Attention Modulation (DSAM) to dynamically adjust feature representations based on the degradation priors Z_0 and Z_1 .

this process of MDSL can be formulated as:

$$\tilde{F}_i = \text{MOS2D}(\text{LN}(F_i)) + F_i, \quad F_{i+1} = \text{CAB}(\text{Conv}(\text{LN}(\tilde{F}_i))) + \tilde{F}_i, \quad (5)$$

where $\text{CAB}(\cdot)$ denotes the Channel Attention Block. $\text{LN}(\cdot)$ represents Layer Normalization.

4.2 Morton-Order 2D-Selective-Scan Module (MOS2D)

To effectively model spatially heterogeneous degradations in 2D images, our MOS2D employs Morton-Order scan, as illustrated in Fig. 1(d). This converts 2D spatial features into locality-preserving 1D sequence, facilitating structured feature interaction and aggregation by SSM.

Specifically, the Morton encoding z maps 2D pixel coordinates (i, j) , where $0 \leq i < H, 0 \leq j < W$, to a 1D index by interleaving the bits of their binary representations. For $i = (i_n, \dots, i_0)_2$ and $j = (j_n, \dots, j_0)_2$, with $n = \lceil \log_2(\max(H, W)) \rceil - 1$, the encoding z is:

$$z = \text{interleave}(i, j) = (j_n, i_n, j_{n-1}, i_{n-1}, \dots, j_1, i_1, j_0, i_0)_2. \quad (6)$$

In the DDEM, Morton-order coding is followed by standard SSM operations to effectively extract global degradation descriptor Z_0 and adaptive degradation kernel Z_1 . In contrast, in our main restoration backbone, the MOS2D module employs degradation-aware modulations using Z_0 and Z_1 through DAFM and DSAM, detailed in Fig. 5. This dual-modulation ensures that the MOS2D is dynamically conditioned on both long range contextually aware and spatially adaptive restoration.

Degradation-Adaptive Feature Modulation (DAFM). The i -th layer's input feature map F_i is first modulated by the global degradation descriptor Z_0 . As shown in Fig. 5, Z_0 is expanded and split to produce channel-wise adaptive weights Z_0^w and biases Z_0^b , which applied to F_i using a feature-wise linear modulation operation, thus incorporates global degradation characteristics:

$$F_{\text{DAFM}} = (Z_0^w \odot F_i) + Z_0^b, \quad Z_0^w, Z_0^b = \text{Split}(\text{Linear}(Z_0)), \quad (7)$$

where \odot denotes element-wise multiplication.

Degradation-Selective Attention Modulation (DSAM). To further guide the S6 Block with local degradation information, the spatially adaptive kernel Z_1 is utilized as follows:

$$F_{\text{DSAM}} = W_F F_{\text{DAFM}} \times \text{Softmax}(W_Z Z_1), \quad (8)$$

where W_F and W_Z are learnable linear projection matrices.

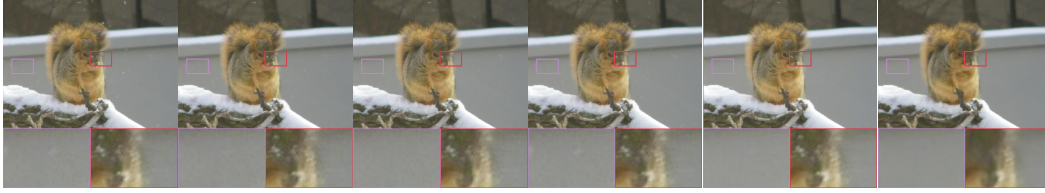
Degradation-Guided S6 Block. The core selective scan operation is performed by our Degradation-Guided S6 Block. Its parameters are dynamically adapted based on the degradation-sensitive features F_{DSAM} derived from the DSAM stage. F_{DSAM} is split into three components, which are then linearly transformed to generate the SSM parameters B , C , and Δ :

$$F_\Delta, F_B, F_C = \text{Split}(F_{\text{DSAM}}), \quad \Delta = W_\Delta F_\Delta, \quad B = W_B F_B, \quad C = W_C F_C, \quad (9)$$

where W_Δ , W_B , and W_C are learnable linear mappings. We use zero-order hold (ZOH) discretization with timescale Δ to obtain the discrete matrices $\bar{A} = e^{\Delta A}$ and $\bar{B} = (\exp(\Delta A) - I)A^{-1}B$, where I is the identity matrix. The S6 Block then processes the Morton-Ordered sequence x_k , which is the Morton-ordered sequence derived from the DAFM features F_{DAFM} , as follows:

$$y_k = C h_k + D x_k, \quad h_k = \bar{A} h_{k-1} + \bar{B} x_k, \quad x_k = F_{\text{DAFM}}[z], \quad (10)$$

where h_k is the hidden state at step k . The dynamically generated B and C (and Δ influencing \bar{A} , \bar{B}) ensure that the state evolution and output generation are adaptive to the degradation characteristics.



(a) Input (b) WGWSNet (c) WeatherDiff (d) Histoformer (e) Histoformer+ (f) Ours

Figure 6: Visual comparison on the real world snow dataset [35]. Compared to the prior methods [78, 44, 54], where “+” denotes additional training of Histoformer, our MODEM achieves superior results without additional training, effectively removing real-world snow and restoring clean details.

Table 1: Quantitative comparison with recent state-of-the-art unified methods [30, 56, 8, 78, 44, 66, 54] across various datasets. The best and second-best results are in **bold** and underlined, respectively.

Methods	Snow100K-S		Snow100K-L		Outdoor		RainDrop		Average	
	PSNR	SSIM								
All-in-One [30]	-	-	28.33	0.8820	24.71	0.8980	31.12	0.9268	28.05	0.9023
TransWeather [56]	32.51	0.9341	29.31	0.8879	28.83	0.9000	30.17	0.9157	30.21	0.9094
Chen <i>et al.</i> [8]	34.42	0.9469	30.22	0.9071	29.27	0.9147	31.81	0.9309	31.43	0.9249
WGWSNet [78]	34.31	0.9460	30.16	0.9007	29.32	0.9207	32.38	0.9378	31.54	0.9263
WeatherDiff ₆₄ [44]	35.83	0.9566	30.09	0.9041	29.64	0.9312	30.71	0.9312	31.57	0.9308
WeatherDiff ₁₂₈ [44]	35.02	0.9516	29.58	0.8941	29.72	0.9216	29.66	0.9225	31.00	0.9225
AWRCP [66]	36.92	0.9652	31.92	0.9341	31.39	0.9329	31.93	0.9314	33.04	0.9409
Histoformer [54]	<u>37.41</u>	<u>0.9656</u>	<u>32.16</u>	0.9261	<u>32.08</u>	<u>0.9389</u>	33.06	0.9441	<u>33.68</u>	<u>0.9437</u>
MODEM (Ours)	38.08	0.9673	32.52	<u>0.9292</u>	33.10	0.9410	<u>33.01</u>	<u>0.9434</u>	34.18	0.9452

4.3 Loss Function

Our model is trained in two stages. In the first stage, the loss $\mathcal{L}_{\text{stage1}}$ combines a \mathcal{L}_1 loss and a correlation loss \mathcal{L}_{cor} to ensure accuracy and structural fidelity between the output of MODEM I_{HQ} and ground-truth I_{GT} :

$$\mathcal{L}_{\text{stage1}} = \mathcal{L}_1(I_{\text{HQ}}, I_{\text{GT}}) + \mathcal{L}_{\text{cor}}(I_{\text{HQ}}, I_{\text{GT}}), \quad (11)$$

The correlation loss $\mathcal{L}_{\text{cor}}(I_{\text{HQ}}, I_{\text{GT}})$ is based on the Pearson correlation coefficient $\rho(I_{\text{HQ}}, I_{\text{GT}})$:

$$\mathcal{L}_{\text{cor}}(I_{\text{HQ}}, I_{\text{GT}}) = \frac{1}{2} (1 - \rho(I_{\text{HQ}}, I_{\text{GT}})), \quad \rho(I_{\text{HQ}}, I_{\text{GT}}) = \frac{\sum_{i=1}^N (I_{i,\text{HQ}} - \bar{I}_{\text{HQ}})(I_{i,\text{GT}} - \bar{I}_{\text{GT}})}{N \cdot \sigma(I_{\text{HQ}}) \cdot \sigma(I_{\text{GT}})}. \quad (12)$$

where N is the total number of pixels, \bar{I} denotes mean, and $\sigma(I)$ denotes standard deviation.

In the second stage, we introduce a KL divergence loss \mathcal{L}_{KL} to maintain consistency of the degradation representation \tilde{Z} across stages. Let $\tilde{Z}_{0,\text{st1}}$ and $\tilde{Z}_{0,\text{st2}}$ be the \tilde{Z} vectors from the first (fixed) and second stages, respectively. The KL divergence is computed between their softmax distributions $\phi(\cdot)$:

$$\mathcal{L}_{\text{KL}} = D_{\text{KL}} \left(\phi(\tilde{Z}_{0,\text{st1}}) \parallel \phi(\tilde{Z}_{0,\text{st2}}) \right) = \sum_{j=1}^{4C_d} \phi(\tilde{Z}_{0,\text{st1}}(j)) \log \left(\frac{\phi(\tilde{Z}_{0,\text{st1}}(j))}{\phi(\tilde{Z}_{0,\text{st2}}(j))} \right). \quad (13)$$

The total loss for the second stage, $\mathcal{L}_{\text{stage2}}$, can be formulated as:

$$\mathcal{L}_{\text{stage2}} = \mathcal{L}_1(I_{\text{HQ}}, I_{\text{GT}}) + \mathcal{L}_{\text{cor}}(I_{\text{HQ}}, I_{\text{GT}}) + \mathcal{L}_{\text{KL}}(\tilde{Z}_{0,\text{st1}}, \tilde{Z}_{0,\text{st2}}). \quad (14)$$

5 Experimental Validation

Our MODEM is implemented in PyTorch [45] and trained on 4 NVIDIA RTX 3090 GPUs in two stages. We employ the AdamW optimizer [37] with a Cosine Annealing Restart Cyclic LR scheduler [36]. It is trained on an all-weather dataset [56, 54], consistent with prior works [30, 56, 44, 54, 78, 66]. For evaluation, MODEM is tested on established benchmarks including Test1 [29, 30], RainDrop [46], Snow100K-L/S [35], and a real-world snow test set [35]. Due to the page limit, more details are given in Appendices A.1 and A.2.

Table 2: Desnowing Task

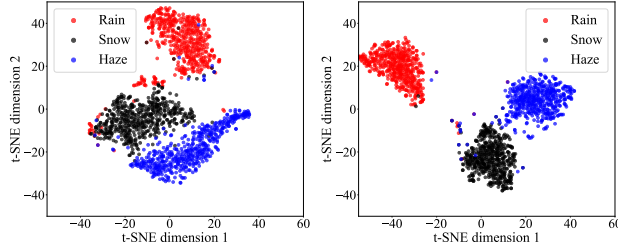
Methods	Snow100K-S		Snow100K-L	
	PSNR	SSIM	PSNR	SSIM
SPANet [58]	29.92	0.8260	23.70	0.7930
JSTASR [7]	31.40	0.9012	25.32	0.8076
RESCAN [31]	31.51	0.9032	26.08	0.8108
DesnowNet [35]	32.33	0.9500	27.17	0.8983
DDMSNet [73]	34.34	0.9445	28.85	0.8772
NAFNet [6]	34.79	0.9497	30.06	0.9017
Restormer [69]	<u>36.01</u>	<u>0.9579</u>	<u>30.36</u>	<u>0.9068</u>
MODEM (Ours)	38.08	0.9673	32.52	0.9292

Table 3: Raindrop Removal Task

Methods	RainDrop	
	PSNR	SSIM
pix2pix [20]	28.02	0.8547
DuRN [33]	31.24	0.9259
RaindropAttn [47]	31.44	0.9263
AttentiveGAN [46]	31.59	0.9170
IDT [61]	31.87	0.9313
MAXIM [55]	31.87	0.9352
Restormer [69]	<u>32.18</u>	<u>0.9408</u>
MODEM (Ours)	33.01	0.9434

Table 4: Deraining & Dehazing Task

Methods	Outdoor-Rain	
	PSNR	SSIM
CycleGAN [76]	17.62	0.6560
pix2pix [20]	19.09	0.7100
HRGAN [29]	21.56	0.8550
PCNet [21]	26.19	0.9015
MPRNet [68]	28.03	0.9192
NAFNet [6]	29.59	0.9027
Restormer [69]	<u>30.03</u>	<u>0.9215</u>
MODEM (Ours)	33.10	0.9410



(g) T-SNE of Histoformer [54]

(h) T-SNE of MODEM

Figure 7: T-SNE results of Histoformer [54] and MODEM, which reflect that MODEM exhibits better clustering of features corresponding to different weather types than Histoformer.

5.1 Comparisons with State-of-the-arts

Quantitative Comparison. Our quantitative evaluation assesses MODEM against both unified models [30, 56, 8, 78, 44, 66, 54] and task-specific methods [58, 7, 31, 35, 73, 6, 69, 33, 20, 47, 46, 61, 55, 76, 29, 21, 68]. As reported in Table 1, MODEM achieves SOTA performance, with an average PSNR improvement of 0.5dB across benchmarks [29, 30, 46, 35], and a notable 1.02dB gain on Outdoor-Rain [29, 30]. While slightly below Histoformer on RainDrop [46] by 0.05dB PSNR, MODEM yields compelling visual results, a point further elaborated in our qualitative comparisons. Furthermore, comparisons with leading task-specific methods in Tables 2 to 4 confirm MODEM consistently attains SOTA results. These evaluations underscore MODEM’s capability to effectively estimate and adapt to diverse, spatially heterogeneous weather degradations. Additionally, the comparisons of complexity can be found in Appendix A.3.

Qualitative comparison. We provide qualitative comparisons across diverse scenarios in Figs. 6 and 8. For image desnowing on Snow100K [35], MODEM effectively removes heavy snowflakes and visual artifacts that other models [78, 44, 54] struggle to address. For joint deraining and dehazing on Outdoor-Rain [29, 30], MODEM excels in restoring richer texture details and produces images with noticeably fewer artifacts. For raindrop removal on the Raindrop [46], MODEM again demonstrates superior detail preservation and artifact reduction. Furthermore, on real-world snowy images [35], MODEM achieves superior results as shown in Fig. 6 even without any additional fine-tuning, showcasing excellent generalization and real-world applicability, which can be attributed to its profound understanding and adaptive modeling of degradation characteristics. More cases can be found in Appendix A.5.

5.2 Ablation Studies

We evaluate the impact of the Morton-Order scan, DDEM, DAFM and DSAM. Morton-Order scan facilitates structured spatial feature processing within the SSM, enabling the model to better capture contextual dependencies and preserve local structural coherence. As shown in Table 5, configurations incorporating the Morton scan generally yield improved performance, underscoring its benefit in organizing spatial information for sequential modeling. DDEM provides the degradation priors Z_0 and Z_1 that guide the DAFM and DSAM. As indicated in Table 5, configurations lacking DDEM exhibit a significant performance drop. DAFM, which utilizes the global degradation prior Z_0 , plays

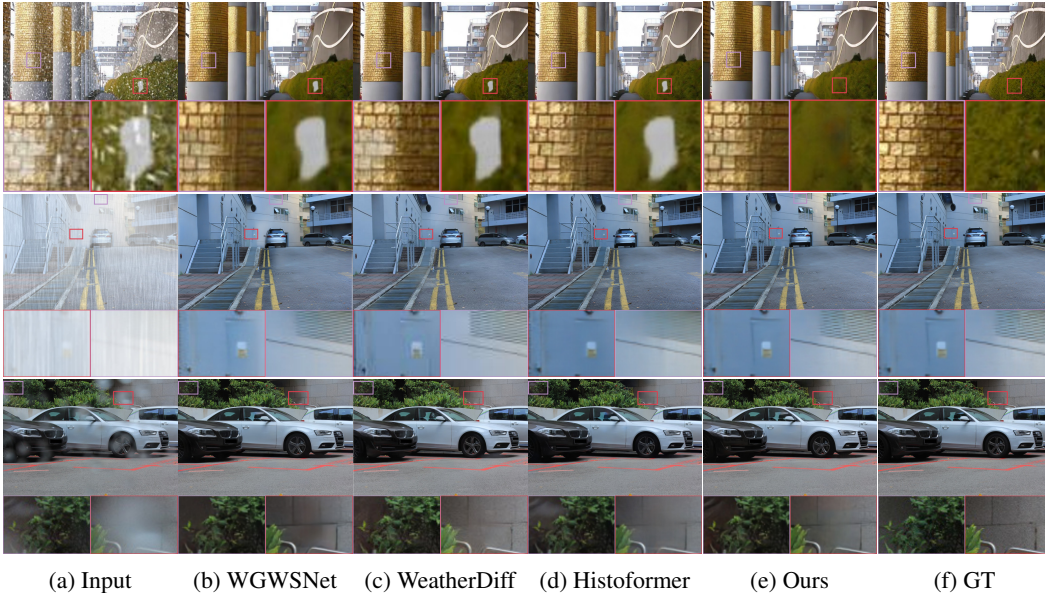


Figure 8: Visual comparisons of MODEM against state-of-the-art unified methods across diverse adverse weather restoration tasks. **Top Row**: Image desnowing. **Middle Row**: Joint deraining and dehazing. **Bottom Row**: Raindrop removal.

Table 5: Ablation study results across different datasets and factor combinations.

Factors				Snow100K-S		Snow100K-L		Outdoor		RainDrop	
Morton	DDEM	DAFM	DSAM	PSNR	SSIM	PSNR	SSIM	PSNR	SSIM	PSNR	SSIM
✗	✓	✓	✓	38.03	0.9672	32.33	0.9283	32.89	0.9399	32.69	0.9423
✓	✗	N/A	N/A	37.61	0.9650	32.12	0.9249	32.37	0.9224	32.38	0.9390
✓	✓	✓	✗	38.15	0.9675	32.59	0.9298	32.77	0.9404	32.72	0.9435
✓	✓	✗	✓	37.43	0.9643	32.07	0.9240	32.19	0.9308	32.62	0.9387
✓	✓	✓	✓	38.08	0.9673	32.52	0.9292	33.10	0.9410	33.01	0.9434

a crucial role in adaptively modulating features based on the overall estimated weather type and severity. DSAM, guided by the spatially adaptive kernel Z_1 , allows the MOS2D to selectively focus on and modulate features pertinent to local degradation characteristics or specific image regions. While removing DSAM shows marginal gains on certain snow metrics, it impairs performance on tasks like raindrop removal, which demands strong local adaptation due to the highly local nature of raindrops, and on mixed rain&haze scenarios where intricate local texture recovery is challenging. Thus, DSAM, guided by the spatially adaptive kernel Z_1 , is crucial for achieving robust, balanced performance across diverse weather conditions by guiding the network to selectively address these local characteristics. The combination of all components employed in full MODEM, consistently yields the best results. This result is further supported by t-SNE [57] in Fig. 7. Compared to Histoformer [54], MODEM exhibits significantly improved clustering of features corresponding to different weather types. This indicates that the combined action of the components enables MODEM to learn more discriminative and well-separated feature representations, which directly contributes to enhance restoration capabilities.

6 Conclusion

In this paper, we introduced the Morton-Order Degradation Estimation Mechanism (MODEM) to address the challenge of restoring images degraded by diverse and spatially heterogeneous adverse weather. MODEM integrates a Dual Degradation Estimation Module (DDEM) for extracting global and local degradation priors, with a Morton-Order 2D-Selective-Scan Module (MOS2D) that employs Morton-coded spatial ordering and selective state-space models for adaptive, context-aware restoration. Extensive experiments demonstrate MODEM’s state-of-the-art performance across multiple benchmarks and weather types. This superiority is attributed to its effective modeling of complex degradation dynamics via explicit degradation estimation guiding the restoration process, leading to more discriminative feature representations and strong generalization to real-world scenarios.

References

- [1] Yasin Almalioglu, Mehmet Turan, Niki Trigoni, and Andrew Markham. Deep learning-based robust positioning for all-weather autonomous driving. *Nature machine intelligence*, 4(9): 749–760, 2022.
- [2] Codruta O. Ancuti and Cosmin Ancuti. Single image dehazing by multi-scale fusion. *IEEE Trans. Image Process.*, 22(8):3271–3282, 2013.
- [3] Jiesong Bai, Yuhao Yin, and Qiyuan He. Retinexmamba: Retinex-based mamba for low-light image enhancement. *arXiv preprint arXiv:2405.03349*, 2024.
- [4] Dana Berman, Tali Treibitz, and Shai Avidan. Non-local image dehazing. In *CVPR*, pages 1674–1682. IEEE Computer Society, 2016.
- [5] Lei Cai, Yuli Fu, Wanliang Huo, Youjun Xiang, Tao Zhu, Ying Zhang, Huanqiang Zeng, and Delu Zeng. Multiscale attentive image de-raining networks via neural architecture search. *IEEE Trans. Circuits Syst. Video Technol.*, 33(2):618–633, 2023. doi: 10.1109/TCSVT.2022.3207516. URL <https://doi.org/10.1109/TCSVT.2022.3207516>.
- [6] Liangyu Chen, Xiaojie Chu, Xiangyu Zhang, and Jian Sun. Simple baselines for image restoration. In *European conference on computer vision*, pages 17–33. Springer, 2022.
- [7] Wei-Ting Chen, Hao-Yu Fang, Jian-Jiun Ding, Cheng-Che Tsai, and Sy-Yen Kuo. Jstasr: Joint size and transparency-aware snow removal algorithm based on modified partial convolution and veiling effect removal. In *Computer Vision—ECCV 2020: 16th European Conference, Glasgow, UK, August 23–28, 2020, Proceedings, Part XXI 16*, pages 754–770. Springer, 2020.
- [8] Wei-Ting Chen, Zhi-Kai Huang, Cheng-Che Tsai, Hao-Hsiang Yang, Jian-Jiun Ding, and Sy-Yen Kuo. Learning multiple adverse weather removal via two-stage knowledge learning and multi-contrastive regularization: Toward a unified model. In *CVPR*, pages 17632–17641. IEEE, 2022.
- [9] Rui Deng and Tianpei Gu. Cu-mamba: Selective state space models with channel learning for image restoration. *arXiv preprint arXiv:2404.11778*, 2024.
- [10] David Eigen, Dilip Krishnan, and Rob Fergus. Restoring an image taken through a window covered with dirt or rain. In *Proceedings of the IEEE international conference on computer vision*, pages 633–640, 2013.
- [11] Xueyang Fu, Jiabin Huang, Delu Zeng, Yue Huang, Xinghao Ding, and John W. Paisley. Removing rain from single images via a deep detail network. In *CVPR*, pages 1715–1723. IEEE Computer Society, 2017.
- [12] Albert Gu and Tri Dao. Mamba: Linear-time sequence modeling with selective state spaces. *arXiv preprint arXiv:2312.00752*, 2023.
- [13] Albert Gu, Karan Goel, and Christopher Ré. Efficiently modeling long sequences with structured state spaces. *arXiv preprint arXiv:2111.00396*, 2021.
- [14] Meisheng Guan, Haiyong Xu, Gangyi Jiang, Mei Yu, Yeyao Chen, Ting Luo, and Yang Song. Watermamba: Visual state space model for underwater image enhancement. *arXiv preprint arXiv:2405.08419*, 2024.
- [15] Hang Guo, Jinmin Li, Tao Dai, Zhihao Ouyang, Xudong Ren, and Shu-Tao Xia. Mambair: A simple baseline for image restoration with state-space model. *arXiv preprint arXiv:2402.15648*, 2024.
- [16] Xiaojie Guo, Yang Yang, Chaoyue Wang, and Jiayi Ma. Image dehazing via enhancement, restoration, and fusion: A survey. *Inf. Fusion*, 86-87:146–170, 2022.
- [17] Zhixiang Hao, Shaodi You, Yu Li, Kunming Li, and Feng Lu. Learning from synthetic photorealistic raindrop for single image raindrop removal. In *Proceedings of the IEEE/CVF International Conference on Computer Vision Workshops*, pages 0–0, 2019.

- [18] Kaiming He, Jian Sun, and Xiaoou Tang. Single image haze removal using dark channel prior. In *CVPR*, pages 1956–1963. IEEE Computer Society, 2009.
- [19] Yongsong Huang, Tomo Miyazaki, Xiaofeng Liu, and Shinichiro Omachi. Irsrmamba: Infrared image super-resolution via mamba-based wavelet transform feature modulation model. *arXiv preprint arXiv:2405.09873*, 2024.
- [20] Phillip Isola, Jun-Yan Zhu, Tinghui Zhou, and Alexei A Efros. Image-to-image translation with conditional adversarial networks. In *Proceedings of the IEEE conference on computer vision and pattern recognition*, pages 1125–1134, 2017.
- [21] Kui Jiang, Zhongyuan Wang, Peng Yi, Chen Chen, Zheng Wang, Xiao Wang, Junjun Jiang, and Chia-Wen Lin. Rain-free and residue hand-in-hand: A progressive coupled network for real-time image deraining. *IEEE Transactions on Image Processing*, 30:7404–7418, 2021.
- [22] Tai-Xiang Jiang, Ting-Zhu Huang, Xi-Le Zhao, Liang-Jian Deng, and Yao Wang. A novel tensor-based video rain streaks removal approach via utilizing discriminatively intrinsic priors. In *CVPR*, pages 2818–2827. IEEE Computer Society, 2017.
- [23] Xin Jin, Haisheng Su, Kai Liu, Cong Ma, Wei Wu, Fei Hui, and Junchi Yan. Unimamba: Unified spatial-channel representation learning with group-efficient mamba for lidar-based 3d object detection. *arXiv preprint arXiv:2503.12009*, 2025.
- [24] Li-Wei Kang, Chia-Wen Lin, and Yu-Hsiang Fu. Automatic single-image-based rain streaks removal via image decomposition. *IEEE Trans. Image Process.*, 21(4):1742–1755, 2012. doi: 10.1109/TIP.2011.2179057. URL <https://doi.org/10.1109/TIP.2011.2179057>.
- [25] Bernhard Kerbl, Georgios Kopanas, Thomas Leimkühler, and George Drettakis. 3d gaussian splatting for real-time radiance field rendering. *ACM Trans. Graph.*, 42(4):139–1, 2023.
- [26] Lingshun Kong, Jiangxin Dong, Ming-Hsuan Yang, and Jinshan Pan. Efficient visual state space model for image deblurring. *arXiv preprint arXiv:2405.14343*, 2024.
- [27] Dong Li, Yidi Liu, Xueyang Fu, Senyan Xu, and Zheng-Jun Zha. Fouriermamba: Fourier learning integration with state space models for image deraining. *arXiv preprint arXiv:2405.19450*, 2024.
- [28] Minghan Li, Xiangyong Cao, Qian Zhao, Lei Zhang, and Deyu Meng. Online rain/snow removal from surveillance videos. *IEEE Trans. Image Process.*, 30:2029–2044, 2021.
- [29] Ruoteng Li, Loong-Fah Cheong, and Robby T Tan. Heavy rain image restoration: Integrating physics model and conditional adversarial learning. In *Proceedings of the IEEE/CVF conference on computer vision and pattern recognition*, pages 1633–1642, 2019.
- [30] Ruoteng Li, Robby T Tan, and Loong-Fah Cheong. All in one bad weather removal using architectural search. In *Proceedings of the IEEE/CVF conference on computer vision and pattern recognition*, pages 3175–3185, 2020.
- [31] Xia Li, Jianlong Wu, Zhouchen Lin, Hong Liu, and Hongbin Zha. Recurrent squeeze-and-excitation context aggregation net for single image deraining. In *Proceedings of the European conference on computer vision (ECCV)*, pages 254–269, 2018.
- [32] Jiaying Liu, Wenhan Yang, Shuai Yang, and Zongming Guo. Erase or fill? deep joint recurrent rain removal and reconstruction in videos. In *CVPR*, pages 3233–3242. Computer Vision Foundation / IEEE Computer Society, 2018.
- [33] Xing Liu, Masanori Suganuma, Zhun Sun, and Takayuki Okatani. Dual residual networks leveraging the potential of paired operations for image restoration. In *Proceedings of the IEEE/CVF conference on computer vision and pattern recognition*, pages 7007–7016, 2019.
- [34] Yue Liu, Yunjie Tian, Yuzhong Zhao, Hongtian Yu, Lingxi Xie, Yaowei Wang, Qixiang Ye, and Yunfan Liu. Vmamba: Visual state space model, 2024. URL <https://arxiv.org/abs/2401.10166>.

- [35] Yun-Fu Liu, Da-Wei Jaw, Shih-Chia Huang, and Jenq-Neng Hwang. Desnownet: Context-aware deep network for snow removal. *IEEE Trans. Image Process.*, 27(6):3064–3073, 2018.
- [36] Ilya Loshchilov and Frank Hutter. Sgdr: Stochastic gradient descent with warm restarts. *arXiv preprint arXiv:1608.03983*, 2016.
- [37] Ilya Loshchilov and Frank Hutter. Decoupled weight decay regularization. *arXiv preprint arXiv:1711.05101*, 2017.
- [38] Jun Ma, Feifei Li, and Bo Wang. U-mamba: Enhancing long-range dependency for biomedical image segmentation. *arXiv preprint arXiv:2401.04722*, 2024.
- [39] Tim Meinhardt, Alexander Kirillov, Laura Leal-Taixe, and Christoph Feichtenhofer. Trackerformer: Multi-object tracking with transformers. In *Proceedings of the IEEE/CVF conference on computer vision and pattern recognition*, pages 8844–8854, 2022.
- [40] Guy M Morton. A computer oriented geodetic data base and a new technique in file sequencing. *IBM, Ottawa, Canada*, 1966.
- [41] Valentina Musat, Ivan Fursa, Paul Newman, Fabio Cuzzolin, and Andrew Bradley. Multi-weather city: Adverse weather stacking for autonomous driving. In *ICCVW*, pages 2906–2915. IEEE, 2021.
- [42] Eric Nguyen, Karan Goel, Albert Gu, Gordon Downs, Preey Shah, Tri Dao, Stephen Baccus, and Christopher Ré. S4nd: Modeling images and videos as multidimensional signals with state spaces. *Advances in neural information processing systems*, 35:2846–2861, 2022.
- [43] Jack A Orenstein and Tim H Merrett. A class of data structures for associative searching. In *Proceedings of the 3rd ACM SIGACT-SIGMOD Symposium on Principles of Database Systems*, pages 181–190, 1984.
- [44] Ozan Özdenizci and Robert Legenstein. Restoring vision in adverse weather conditions with patch-based denoising diffusion models. *IEEE Trans. Pattern Anal. Mach. Intell.*, 45(8):10346–10357, 2023. doi: 10.1109/TPAMI.2023.3238179. URL <https://doi.org/10.1109/TPAMI.2023.3238179>.
- [45] A Paszke. Pytorch: An imperative style, high-performance deep learning library. *arXiv preprint arXiv:1912.01703*, 2019.
- [46] Rui Qian, Robby T. Tan, Wenhan Yang, Jiajun Su, and Jiaying Liu. Attentive generative adversarial network for raindrop removal from a single image. In *CVPR*, pages 2482–2491. Computer Vision Foundation / IEEE Computer Society, 2018.
- [47] Yuhui Quan, Shijie Deng, Yixin Chen, and Hui Ji. Deep learning for seeing through window with raindrops. In *Proceedings of the IEEE/CVF International Conference on Computer Vision*, pages 2463–2471, 2019.
- [48] Weihong Ren, Jiandong Tian, Zhi Han, Antoni B. Chan, and Yandong Tang. Video desnowing and deraining based on matrix decomposition. In *CVPR*, pages 2838–2847. IEEE Computer Society, 2017.
- [49] Stefan Roth and Michael J. Black. Fields of experts: A framework for learning image priors. In *CVPR (2)*, pages 860–867. IEEE Computer Society, 2005.
- [50] Leonid I Rudin, Stanley Osher, and Emad Fatemi. Nonlinear total variation based noise removal algorithms. *Physica D: nonlinear phenomena*, 60(1-4):259–268, 1992.
- [51] Yuanjie Shao, Lerenhan Li, Wenqi Ren, Changxin Gao, and Nong Sang. Domain adaptation for image dehazing. In *CVPR*, pages 2805–2814. Computer Vision Foundation / IEEE, 2020.
- [52] Yuan Shi, Bin Xia, Xiaoyu Jin, Xing Wang, Tianyu Zhao, Xin Xia, Xuefeng Xiao, and Wenming Yang. Vmambair: Visual state space model for image restoration. *arXiv preprint arXiv:2403.11423*, 2024.

- [53] Yuheng Shi, Minjing Dong, Mingjia Li, and Chang Xu. Vssd: Vision mamba with non-causal state space duality. *arXiv preprint arXiv:2407.18559*, 2024.
- [54] Shangquan Sun, Wenqi Ren, Xinwei Gao, Rui Wang, and Xiaochun Cao. Restoring images in adverse weather conditions via histogram transformer. In *European Conference on Computer Vision*, pages 111–129. Springer, 2024.
- [55] Zhengzhong Tu, Hossein Talebi, Han Zhang, Feng Yang, Peyman Milanfar, Alan Bovik, and Yinxiao Li. Maxim: Multi-axis mlp for image processing. In *Proceedings of the IEEE/CVF conference on computer vision and pattern recognition*, pages 5769–5780, 2022.
- [56] Jeya Maria Jose Valanarasu, Rajeev Yasarla, and Vishal M Patel. Transweather: Transformer-based restoration of images degraded by adverse weather conditions. In *Proceedings of the IEEE/CVF conference on computer vision and pattern recognition*, pages 2353–2363, 2022.
- [57] Laurens Van der Maaten and Geoffrey Hinton. Visualizing data using t-sne. *Journal of machine learning research*, 9(11), 2008.
- [58] Tianyu Wang, Xin Yang, Ke Xu, Shaozhe Chen, Qiang Zhang, and Rynson WH Lau. Spatial attentive single-image deraining with a high quality real rain dataset. In *Proceedings of the IEEE/CVF conference on computer vision and pattern recognition*, pages 12270–12279, 2019.
- [59] Zhengwei Wang, Qi She, and Aljosa Smolic. Action-net: Multipath excitation for action recognition. In *CVPR*, pages 13214–13223. Computer Vision Foundation / IEEE, 2021.
- [60] Haiyan Wu, Yanyun Qu, Shaohui Lin, Jian Zhou, Ruizhi Qiao, Zhizhong Zhang, Yuan Xie, and Lizhuang Ma. Contrastive learning for compact single image dehazing. In *CVPR*, pages 10551–10560. Computer Vision Foundation / IEEE, 2021.
- [61] Jie Xiao, Xueyang Fu, Aiping Liu, Feng Wu, and Zheng-Jun Zha. Image de-raining transformer. *IEEE transactions on pattern analysis and machine intelligence*, 45(11):12978–12995, 2022.
- [62] Wenhan Yang, Robby T. Tan, Jiashi Feng, Zongming Guo, Shuicheng Yan, and Jiaying Liu. Joint rain detection and removal from a single image with contextualized deep networks. *IEEE Trans. Pattern Anal. Mach. Intell.*, 42(6):1377–1393, 2020.
- [63] Yang Yang, Chun-Le Guo, and Xiaojie Guo. Depth-aware unpaired video dehazing. *IEEE Trans. Image Process.*, 33:2388–2403, 2024.
- [64] Yang Yang, Chaoyue Wang, Xiaojie Guo, and Dacheng Tao. Robust unpaired image dehazing via density and depth decomposition. *Int. J. Comput. Vis.*, 132(5):1557–1577, 2024.
- [65] Rajeev Yasarla and Vishal M. Patel. Uncertainty guided multi-scale residual learning-using a cycle spinning CNN for single image de-raining. In *CVPR*, pages 8405–8414. Computer Vision Foundation / IEEE, 2019.
- [66] Tian Ye, Sixiang Chen, Jinbin Bai, Jun Shi, Chenghao Xue, Jingxia Jiang, Junjie Yin, Erkang Chen, and Yun Liu. Adverse weather removal with codebook priors. In *Proceedings of the IEEE/CVF international conference on computer vision*, pages 12653–12664, 2023.
- [67] Shaodi You, Robby T Tan, Rei Kawakami, Yasuhiro Mukaigawa, and Katsushi Ikeuchi. Adherent raindrop modeling, detection and removal in video. *IEEE transactions on pattern analysis and machine intelligence*, 38(9):1721–1733, 2015.
- [68] Syed Waqas Zamir, Aditya Arora, Salman Khan, Munawar Hayat, Fahad Shahbaz Khan, Ming-Hsuan Yang, and Ling Shao. Multi-stage progressive image restoration. In *Proceedings of the IEEE/CVF conference on computer vision and pattern recognition*, pages 14821–14831, 2021.
- [69] Syed Waqas Zamir, Aditya Arora, Salman Khan, Munawar Hayat, Fahad Shahbaz Khan, and Ming-Hsuan Yang. Restormer: Efficient transformer for high-resolution image restoration. In *Proceedings of the IEEE/CVF conference on computer vision and pattern recognition*, pages 5728–5739, 2022.

- [70] He Zhang and Vishal M Patel. Density-aware single image de-raining using a multi-stream dense network. In *Proceedings of the IEEE conference on computer vision and pattern recognition*, pages 695–704, 2018.
- [71] Jingang Zhang, Wenqi Ren, Shengdong Zhang, He Zhang, Yunfeng Nie, Zhe Xue, and Xiaochun Cao. Hierarchical density-aware dehazing network. *IEEE Trans. Cybern.*, 52(10):11187–11199, 2022.
- [72] Kaihao Zhang, Dongxu Li, Wenhan Luo, and Wenqi Ren. Dual attention-in-attention model for joint rain streak and raindrop removal. *IEEE Transactions on Image Processing*, 30:7608–7619, 2021.
- [73] Kaihao Zhang, Rongqing Li, Yanjiang Yu, Wenhan Luo, and Changsheng Li. Deep dense multi-scale network for snow removal using semantic and depth priors. *IEEE Trans. Image Process.*, 30:7419–7431, 2021.
- [74] Xuanqi Zhang, Haijin Zeng, Jinwang Pan, Qiangqiang Shen, and Yongyong Chen. Llemamba: Low-light enhancement via relighting-guided mamba with deep unfolding network. *arXiv preprint arXiv:2406.01028*, 2024.
- [75] Zou Zhen, Yu Hu, and Zhao Feng. Freqmamba: Viewing mamba from a frequency perspective for image deraining. *arXiv preprint arXiv:2404.09476*, 2024.
- [76] Jun-Yan Zhu, Taesung Park, Phillip Isola, and Alexei A Efros. Unpaired image-to-image translation using cycle-consistent adversarial networks. In *Proceedings of the IEEE international conference on computer vision*, pages 2223–2232, 2017.
- [77] Lianghai Zhu, Bencheng Liao, Qian Zhang, Xinlong Wang, Wenyu Liu, and Xinggang Wang. Vision mamba: Efficient visual representation learning with bidirectional state space model. *arXiv preprint arXiv:2401.09417*, 2024.
- [78] Yurui Zhu, Tianyu Wang, Xueyang Fu, Xuanyu Yang, Xin Guo, Jifeng Dai, Yu Qiao, and Xiaowei Hu. Learning weather-general and weather-specific features for image restoration under multiple adverse weather conditions. In *CVPR*, pages 21747–21758. IEEE, 2023.

A Appendix

A.1 Implement Details

MODEM is implemented in PyTorch [45] and trained on 4 NVIDIA RTX 3090 GPUs. The main backbone contains residual groups with [4, 4, 6, 8, 6, 4, 4] MDSLs sequentially, and a final refinement group with 4 MDSLs. Downsampling and upsampling are performed using PixelUnshuffle and PixelShuffle, respectively. The initial channel size is 36. The DDEM employs residual groups with 2 MDSLs each, operating with 96 channels. We train MODEM in two stages. In Stage 1, DDEM takes the channel-concatenated degraded image I_{LQ} and ground-truth I_{GT} as input. We use the AdamW optimizer [37] with a learning rate of 3×10^{-4} , a weight decay of 1×10^{-4} , and betas set to (0.9, 0.999). The learning rate is scheduled by a Cosine Annealing Restart Cyclic LR [36] scheduler with periods of [92k, 208k] iterations and restart weights of [1, 1]. The minimum learning rates, η_{min} , for these cycles are [3×10^{-4} , 1×10^{-6}]. Progressive training is adopted with patch sizes [128, 160, 256, 320, 384] and corresponding per-GPU mini-batch sizes [6, 4, 2, 1, 1] for [92k, 84k, 56k, 36k, 32k] iterations each, totaling 300k iterations. In Stage 2, DDEM processes only I_{LQ} , initializing parameters from Stage 1. The same AdamW optimizer settings and Cosine Annealing Restart Cyclic LR scheduler parameters are employed. Progressive training uses patch sizes [128, 160, 256, 320, 376] with per-GPU mini-batch sizes [8, 5, 2, 1, 1].

A.2 Datasets and Metrics

To ensure a fair and comprehensive evaluation, MODEM is trained and tested consistent with those utilized in prior works [30, 56, 44, 54, 78, 66]. Our composite training data is aggregated from multiple sources, including 9,000 synthetic images featuring snow degradation from Snow100K [35], 1,069 real-world images affected by adherent raindrops from the Raindrop [46], and an additional 9,000 synthetic images from Outdoor-Rain [29] which are degraded by a combination of both fog and rain streaks. For performance evaluation, we utilize several distinct test sets: the Test1 [29, 30], the designated test split from the RainDrop [46], both the Snow100K-L and Snow100K-S subsets [35], and a challenging real-world test set from Snow100K comprising 1,329 images captured under various adverse weather conditions. We report PSNR and SSIM on these test datasets.

A.3 Complexity Analysis

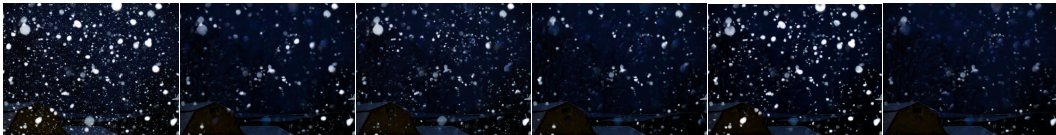
We report the parameters and inference time. The inference time is performed on a single Nvidia RTX 3090, with single 256×256 input image, detailed in Table 6.

Table 6: Comparison of parameters and inference time, along with average PSNR.

Methods	WGWSNet	WeatherDiff	Histoformer	MODEM
Time (ms)	24.83	1.67×10^6	109.07	92.86
Parameters (M)	2.65	82.96	16.62	19.96
Average PSNR	31.54	31.57	33.68	34.18

A.4 Limitations

While our proposed MODEM demonstrates state-of-the-art performance across a variety of adverse weather conditions, we acknowledge certain limitations. As illustrated in Fig. 9 of challenging real-world snow scenarios, MODEM, like other contemporary methods, can encounter difficulties in achieving perfect restoration when faced with images containing extremely large, high-contrast snowflakes. Such scenarios are particularly challenging if these specific visual patterns of snow, differing significantly in scale, density, or opacity from typical training examples, are underrepresented



(a) Input (b) WGWSNet (c) WeatherDiff (d) Histoformer (e) Histoformer+ (f) Ours

Figure 9: Visual comparison on a challenging real-world snow case from the dataset in [35], illustrating performance under severe degradation unseen during training. We compare MODEM to the prior methods [78, 44, 54], where “+” denotes additional training of Histoformer.

or entirely absent in the training data distribution. Nevertheless, empowered by its robust degradation estimation capabilities, MODEM still achieves comparatively better results in these extreme cases, effectively suppressing artifacts and preserving some structural detail. This highlights an ongoing challenge in achieving perfect generalization to all unseen severe degradations, but also underscores the significant benefit of incorporating explicit and adaptive degradation estimation.

A.5 More Visual Comparisons

Further visual comparisons are presented in Figs. 10 to 13.

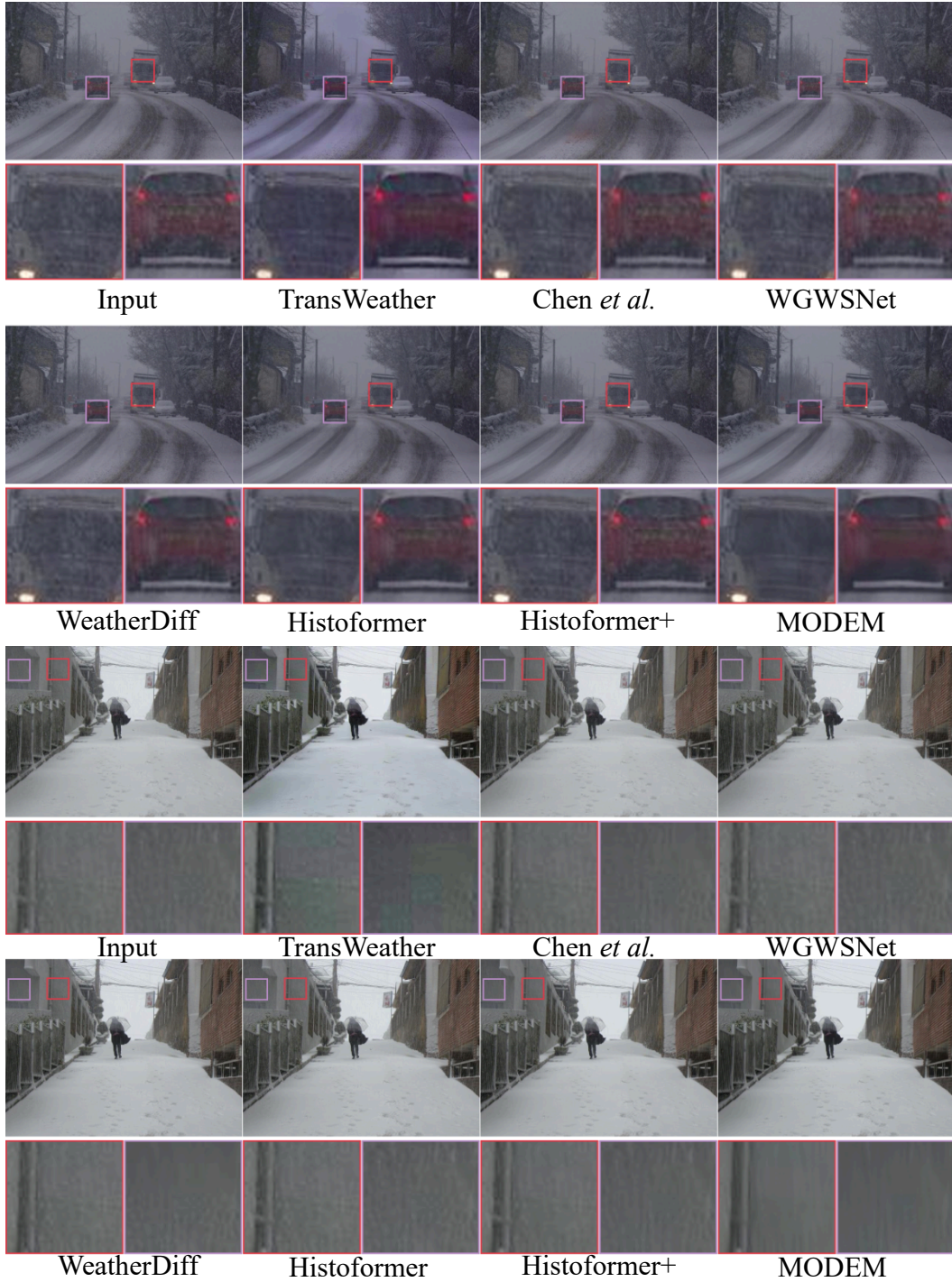


Figure 10: More visual results for desnowing on real-world snowy images [35].

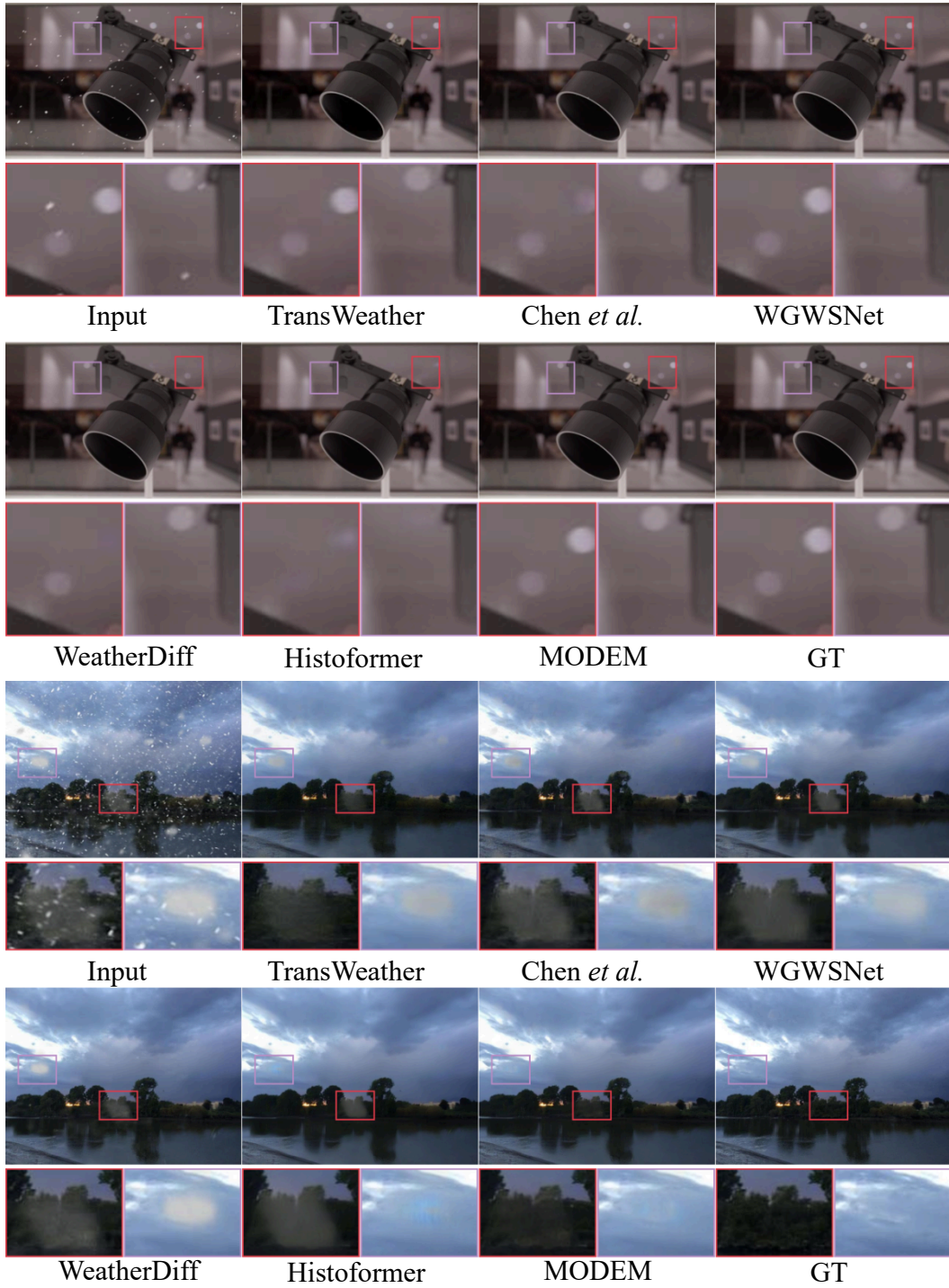


Figure 11: More visual results for image desnowing on the Snow100K [35].

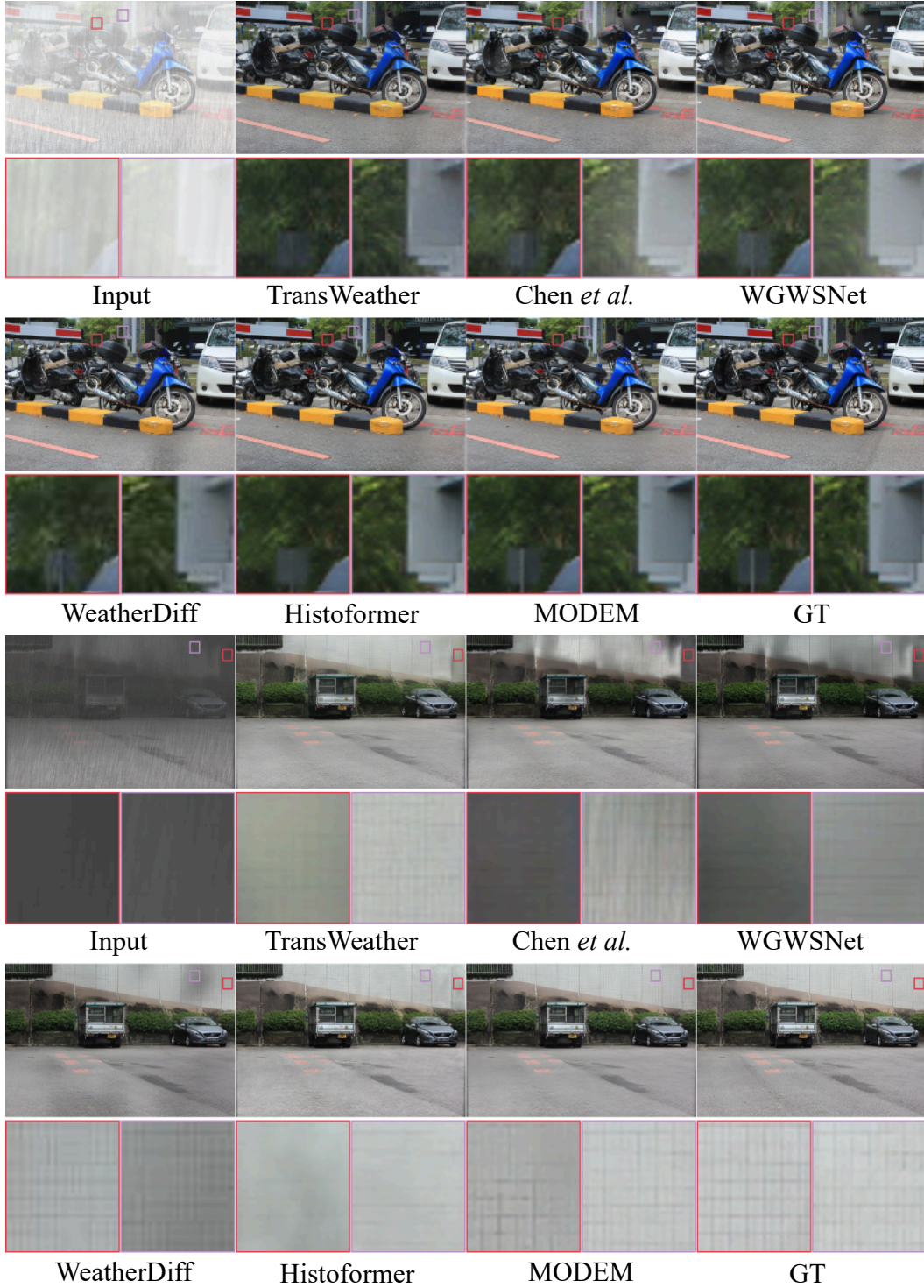


Figure 12: More visual results for deraining&dehazing on the Test1 dataset [29, 30].

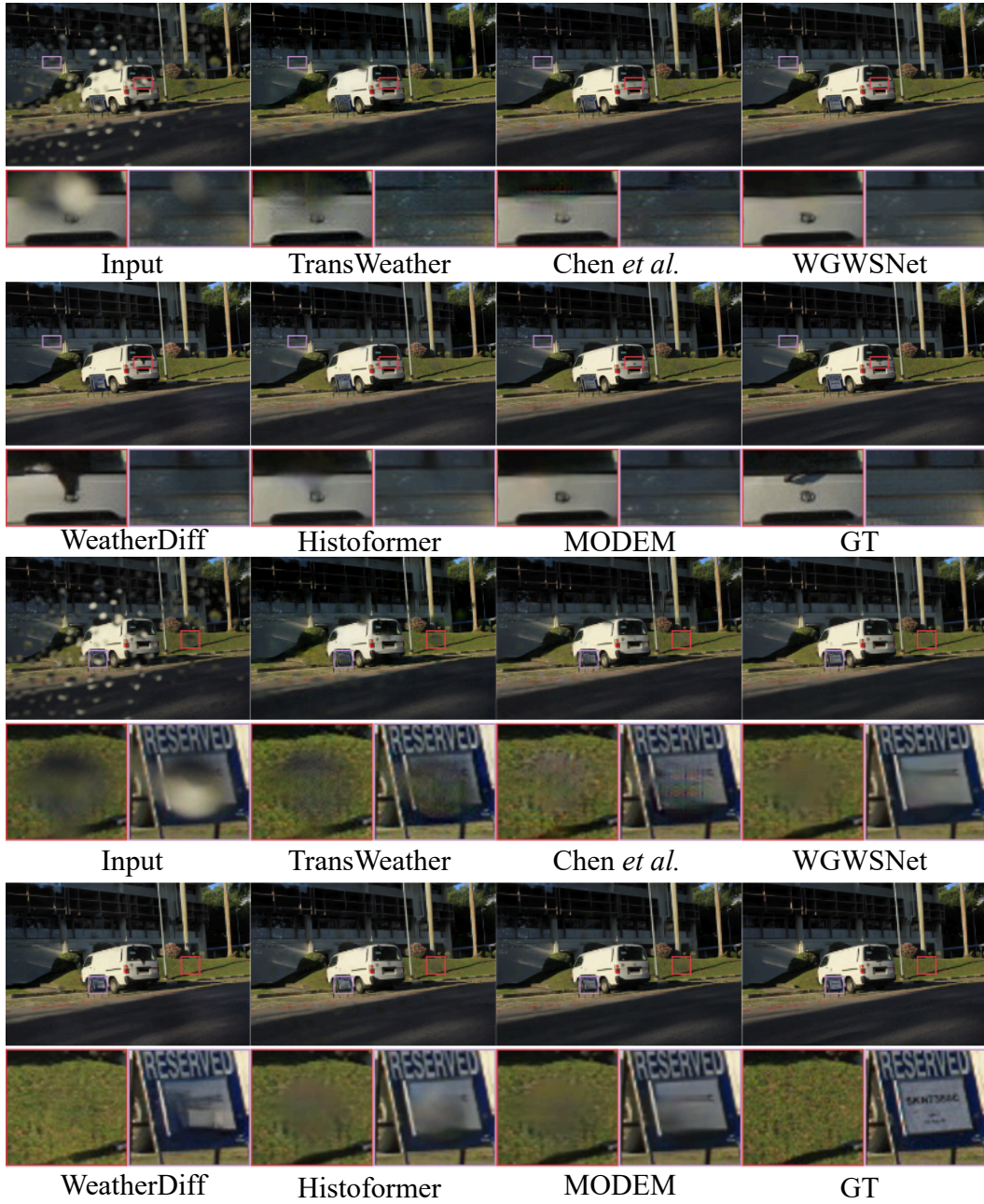


Figure 13: More visual results for raindrop removal on the Raindrop dataset [46].